CrossMark

J. Fluid Mech. (2016), *vol.* 809, *pp.* 873–894. © Cambridge University Press 2016
doi:10.1017/jfm.2016.691

Stability of slender inverted flags and rods in uniform steady flow

John E. Sader[1,2,†], Cecilia Huertas-Cerdeira[3] and Morteza Gharib[3]

[1]School of Mathematics and Statistics, The University of Melbourne, Victoria 3010, Australia

[2]Department of Physics, California Institute of Technology, Pasadena, CA 91125, USA

[3]Division of Engineering and Applied Science, California Institute of Technology, Pasadena, CA 91125, USA

(Received 2 June 2016; revised 10 October 2016; accepted 12 October 2016; first published online 21 November 2016)

Cantilevered elastic sheets and rods immersed in a steady uniform flow are known to undergo instabilities that give rise to complex dynamics, including limit cycle behaviour and chaotic motion. Recent work has examined their stability in an inverted configuration where the flow impinges on the free end of the cantilever with its clamped edge downstream: this is commonly referred to as an 'inverted flag'. Theory has thus far accurately captured the stability of wide inverted flags only, i.e. where the dimension of the clamped edge exceeds the cantilever length; the latter is aligned in the flow direction. Here, we theoretically examine the stability of slender inverted flags and rods under steady uniform flow. In contrast to wide inverted flags, we show that slender inverted flags are never globally unstable. Instead, they exhibit bifurcation from a state that is globally stable to multiple equilibria of varying stability, as flow speed increases. This theory is compared with new and existing measurements on slender inverted flags and rods, where excellent agreement is observed. The findings of this study have significant implications to investigations of biological phenomena such as the motion of leaves and hairs, which can naturally exhibit a slender geometry with an inverted configuration.

Key words: aerodynamics, flow–structure interactions

1. Introduction

Interaction of an elastic structure with a flowing fluid can generate a broad array of instabilities and dynamics, such as those captured by Schmitz (1941), Kornecki, Dowell & O'Brien (1976), Blackburn & Henderson (1996), Zhang *et al.* (2000), Williamson & Govardhan (2004), Gabbai & Benaroya (2005), Eloy *et al.* (2008), Paidoussis, Price & De Langre (2010), Shelley & Zhang (2011), Luhar & Nepf (2011) and Tadrist, Saudreau & De Langre (2014). These investigations are of importance not only from a fundamental perspective but are critical in engineering, where they can dictate structural integrity. One such problem is the flutter of a thin and flat elastic sheet (i.e. a plate) in a steady uniform flow (Theodorsen 1935; Kornecki *et al.* 1976),

† Email address for correspondence: jsader@unimelb.edu.au

https://doi.org/10.1017/jfm.2016.691 Published online by Cambridge University Press

which is relevant to a host of applications including the prediction of airplane wing stability and understanding the flutter of flags in a steady breeze.

Flags commonly orient themselves in the direction of flow, leading to a configuration where their free end is downstream (Luhar & Nepf 2011). This conventional configuration can lead to rich dynamics, whose complexity is yet to be fully understood despite its ubiquity in nature (Shelley & Zhang 2011). Most recently, some emphasis has been placed on examining the effects of flag orientation on the resulting dynamics and stability. In particular, the inverted configuration, where the flow is reversed and impinges on the free end of the flag, has been explored in several studies. These include slender cantilevered rods (Rinaldi & Paidoussis 2012) and thin cantilevered elastic sheets or flags (Kim *et al.* 2013); 'flag' and 'sheet' shall be used interchangeably in this article. Note that these structures always exhibit finite bending rigidity which is critical to their stability (Shelley & Zhang 2011). The distinction used here between a 'sheet' and a 'rod' is that the cross-section of a sheet contains one geometric dimension that is small relative to the other, e.g. its thickness relative to its width (denoted 'height' in this article, see figure 1). Strikingly different dynamics are observed relative to the conventional flag configuration. Perhaps most intriguingly, the inverted flag exhibits flapping over a finite band of flow speeds with an amplitude comparable with the sheet length (Kim *et al.* 2013). This behaviour has been computationally simulated in several recent reports (Gilmanov, Le & Sotiropoulos 2015; Gurugubelli & Jaiman 2015; Ryu *et al.* 2015; Tang, Liu & Lu 2015). The physical mechanisms leading to this behaviour were explored in a very recent study (Sader *et al.* 2016), showing that large-amplitude flapping is a vortex-induced vibration, a high-Reynolds-number phenomenon, which is described in the next paragraph. Indeed, computational simulations demonstrate that flapping vanishes for Reynolds numbers below ≈ 50 (Ryu *et al.* 2015).

Large-amplitude flapping of an inverted flag occurs at finite flow speed, and starts abruptly as the flow speed increases from zero; similarly, flapping subsequently ceases at a higher critical flow speed. We now summarise the known mechanisms underlying this behaviour. Flapping is initiated by a divergence instability of the zero-deflection equilibrium, i.e. the flag becomes linearly unstable due to hydrodynamic lift forces balancing the elastic restoring force of the sheet. Divergence instability was originally suggested by Kim *et al.* (2013) on experimental grounds, demonstrated computationally by Gurugubelli & Jaiman (2015) and proved mathematically by Sader *et al.* (2016). Sader *et al.* (2016) showed that reducing the sheet's aspect ratio (height/length, with length in the flow direction, see figure 1) decreases the hydrodynamic lift force, causing the divergence instability to occur at higher flow speed. The divergence instability causes the sheet to deflect and present a sharp leading edge to the impinging flow at finite angle of attack. The flow thus separates, generating unsteady vortex shedding that synchronises with the sheet oscillation to produce the flapping motion, i.e. it gives rise to a vortex-induced vibration of the structure. A scaling analysis shows that this can only occur for heavy fluid loading, which is the case considered by Kim *et al.* (2013). This flapping motion ceases at higher flow speed when the natural vortex shedding frequency significantly exceeds the resonant frequency of the sheet, leading to desynchronisation (Sader *et al.* 2016). Gurugubelli & Jaiman (2015) suggest this cessation of flapping at high flow speed is due to the sudden emergence of a deflected equilibrium state. However, measurements show that such an equilibrium always exists within the flapping band; see figure 7 of Sader *et al.* (2016). Therefore, the suggested mechanism of Gurugubelli & Jaiman (2015) for flapping cessation at high flow speed does not explain the phenomenon.

https://doi.org/10.1017/jfm.2016.691 Published online by Cambridge University Press

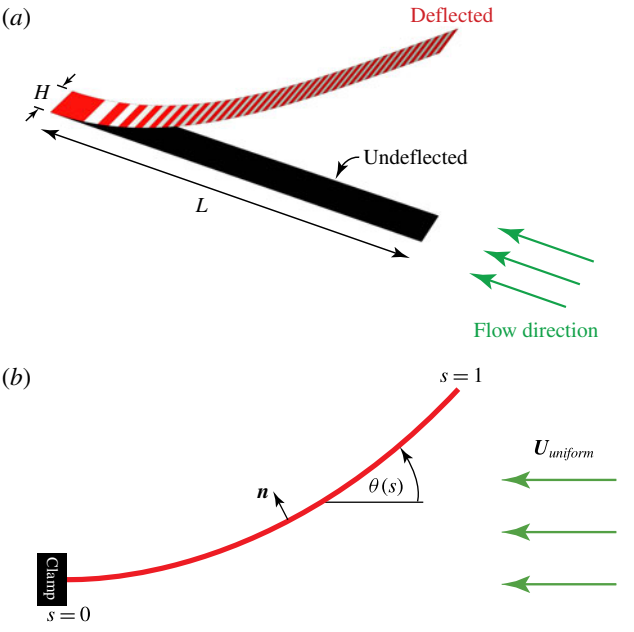

FIGURE 1. (Colour online) Schematic of fluid–structure problem for a slender inverted cantilever sheet in a steady uniform flow. (*a*) Perspective showing geometry of cantilevered sheet and its height, H, length, L, and the flow direction. The sheet thickness, h, is infinitesimally small relative to H and L. Deflected and undeflected sheets are illustrated to indicate the bending mode under investigation. The clamp is at the trailing edge. (*b*) Side view of perspective in (*a*) showing direct of uniform flow velocity, $\boldsymbol{U}_{uniform}$, the dimensionless arc length parameter, $s \equiv s_*/L$ (see (2.3)), local deflection angle, θ, and the local unit normal to the sheet $\boldsymbol{n}$ along the cantilevered sheet (red curve). Gravity is along the height direction of the inverted flag (sheet) in the experiments performed in this study, i.e. it points into the page in (*b*); flag dynamics are observed as in (*b*) with the camera positioned above the flag. In the study of Rinaldi & Paidoussis (2012), gravity points in the opposite direction to the flow vector, $\boldsymbol{U}_{uniform}$.

Strikingly, such a vortex-induced vibration is not observed for small aspect ratios with the sheet deflecting suddenly from its stable zero-deflection equilibrium to a stable deflected equilibrium with increasing flow speed.

Mathematical calculation of a divergence instability was performed for thin sheets of large aspect ratio (greater than unity) and assessed by comparison with measurements (Sader *et al.* 2016). Good agreement was observed within measurement uncertainty for aspect ratios larger than one, with no adjustable parameters. Applying the same large-aspect-ratio theory (2.12) to measurements of small-aspect-ratio sheets revealed strong differences; see data comparison in figure 6 of Sader *et al.* (2016) that is reproduced here in figure 5.

In a related study, Rinaldi & Paidoussis (2012) explored the stability of slender, i.e. small-aspect-ratio, inverted rods of circular cross-section in a steady uniform flow. The rods were oriented vertically in a gravitational field. Their theoretical analysis suggested that the rods also exhibit a divergence instability. But again, strong differences were reported in comparison with measurement, though the reason for these discrepancies was not identified. The theoretically predicted flow speeds for instability are two times greater than those measured.

https://doi.org/10.1017/jfm.2016.691 Published online by Cambridge University Press

As such, both Rinaldi & Paidoussis (2012) and Sader *et al.* (2016) observed that the critical flow speeds at which slender inverted flags and rods become unstable are overestimated by the above-mentioned theories that predict a divergence instability. That is, for a given flow speed, the true destabilising hydrodynamic lift force must be larger than that predicted theoretically. This led Sader *et al.* (2016) to speculate on the existence of a vortex-lift mechanism, which is known to increase lift on slender structures (Anderson 1991).

Here, we explore this possibility by conducting a detailed theoretical analysis that rigorously accounts for the hydrodynamic load generated by a slender structure. For this purpose, we draw on the work of Bollay (1939) and Taylor (1952) who calculated the steady hydrodynamic forces on rigid slender rectangular blades and circular cylinders, respectively. The long axes of the structures are aligned in the flow direction. These previous studies show that, in the asymptotic limit of zero aspect ratio and infinite Reynolds number, the structures do not experience a linear lift force. Incidence at non-zero angle of attack always leads to vortex shedding at finite angle to the structure's side edge. This is in contrast to a large-aspect-ratio sheet that is well modelled using Prandtl's lifting line theory (Jones 1990; Drela 2014). Consequently, the hydrodynamic load experienced by these slender structures, in the limit of extreme slenderness, depends quadratically on the angle of attack, precluding the existence of a linear divergence instability. As we shall show, this flow physics ensures that the zero-deflection equilibrium is never linearly unstable, but gives rise to a saddle-node bifurcation as flow speed increases. This leads to the emergence of multiple stable states that can cause the elastic structure to exhibit intermittent dynamics, depending on the time-dependent nature of the flow and the structure's initial configuration.

The predictions of this theoretical analysis are compared with new measurements on slender inverted flags that verify the existence of these previously unobserved equilibria. This is performed as a function of aspect ratio to examine the interplay of linear and nonlinear lift: a small linear lift component is always present at small and finite (non-zero) aspect ratio (Bollay 1939). The measurements reported by Rinaldi & Paidoussis (2012) for slender inverted rods are also reanalysed using this new theoretical framework, where we now find excellent agreement between theory and measurement.

The present theory for stability of the zero-deflection equilibrium of a slender inverted flag is also connected to the large-aspect-ratio formula (2.12) that was reported by Sader *et al.* (2016). This generates a universal formula (2.15) that is valid for all aspect ratios. This new formula is compared with the measured data of Sader *et al.* (2016), for aspect ratios ranging from small to large, where excellent agreement is observed. As such, this clarifies and eliminates the discrepancy observed by Sader *et al.* (2016) for small aspect ratios (see figure 5).

We begin by reviewing the theoretical model of Bollay (1939) for the hydrodynamic flow and force generated by a straight, slender and thin rigid blade. This is used to develop a rigorous theoretical model for the stability of a slender inverted flag, in the asymptotic limit of zero aspect ratio. The properties of this model, and thus of the flag, are then explored using a simplified rigid sheet model that provides significant insight into the stability landscape. Stability of the zero-deflection equilibrium of a slender inverted flag, calculated using the rigorous model, is then connected with the large-aspect-ratio theory of Sader *et al.* (2016) and a general formula (2.15) is derived for arbitrary aspect ratio. Predictions of the theoretical models are assessed in § 3, where a comparison with detailed measurements on inverted flags is provided. Finally, using

https://doi.org/10.1017/jfm.2016.691 Published online by Cambridge University Press

the present framework we theoretically analyse the inverted rod studied by Rinaldi & Paidoussis (2012), which is vertically aligned in a gravitational field, and present a comparison with their reported measurements.

2. Theoretical model for slender inverted flag

Bollay (1939) calculated the hydrodynamic load experienced by a rigid, straight and thin rectangular blade of small aspect ratio. In the limit of zero aspect ratio, Bollay showed that the normal force coefficient per unit length is

$$C_N = 2\sin^2\theta, \tag{2.1}$$

where the force per length is $N = (1/2)\rho U^2 H C_N$, ρ is the fluid density and U is the speed of the flow that impinges on the blade. Here, θ is the angle of attack of the blade to the impinging flow and H is the blade height (perpendicular to the flow direction). The term 'height', rather than 'span' or 'width', is used here for consistency with Sader *et al.* (2016); see figure 1. The aspect ratio of the blade is the ratio of its height to its length, i.e. H/L, and the blade's thickness is infinitesimally small relative to its height. Bollay (1939) compared this formula with available measurements for $0 \leqslant \theta \leqslant 50°$, where good agreement was observed. Importantly, equation (2.1) also holds for blades at normal incidence, i.e. where the blade length is perpendicular to the flow, $\theta = 90°$ (Goldstein 1965; Batchelor 1974). As such, equation (2.1) is expected to be valid for all angles of attack. It is used here to analyse the behaviour of an inverted flag in the small-aspect-ratio limit. Note that the force per unit length, N, can be expressed equivalently as

$$N = \rho U_n^2 H, \tag{2.2}$$

where U_n is the magnitude of the impinging velocity component normal to the blade.

Equations (2.1) and (2.2) are used in the next section to investigate the stability of the inverted flag; a schematic of this fluid–structure problem is given in figure 1.

2.1. *Equilibrium states*

The nonlinear dependence of (2.1) on the angle of attack, θ, arises from vortex shedding at finite angle to the blade's surface, which always occurs for blades of small aspect ratio. This is an unsteady process and the hydrodynamic force is therefore strictly time-dependent. Equation (2.1) thus specifies a time-averaged force experienced by the blade. Since this equation provides the foundation for our analysis of the inverted flag's deformation, we focus on evaluation of its (steady) equilibrium states. Unsteadiness in the flow will drive the inverted flag away from these equilibrium states and may affect their stability; this is discussed in the next section.

We therefore utilise the equilibrium theory for a slender cantilevered elastic sheet to investigate the deformation of a slender inverted flag in a steady uniform flow; the same elastic deformation theory holds for slender rods and sheets. Arbitrarily large deflections are allowed in this formulation, provided the elastic strains are small. The inverted flag or rod is assumed to have a uniform and symmetric cross-section along its length, L, e.g. a rectangular cross-section (of infinitesimal thickness) considered here or a circular cross-section studied in § 4. It will undergo pure bending when an external force is applied with identical symmetry. This occurs when the slender sheet

https://doi.org/10.1017/jfm.2016.691 Published online by Cambridge University Press

deflects under a uniform steady flow. In such a case, the local rotation angle of the sheet, $\theta(s)$ (see figure 1), satisfies the dimensional equilibrium equation (Landau & Lifshitz 1970),

$$EI\frac{\mathrm{d}^2\theta}{\mathrm{d}s_*^2} = -\boldsymbol{n}(s_*)\cdot\int_{s_*}^{L}\boldsymbol{F}(l_*)\,\mathrm{d}l_*, \tag{2.3}$$

where s_* (and the equivalent integration variable l_*) is the dimensional arc-length along the sheet ($s_* = 0$ at the clamped end), E is the Young's modulus of the sheet, I is its areal moment of inertia, $\boldsymbol{F}$ is the local applied force per unit length and $\boldsymbol{n}$ is the local unit normal to the sheet's axis at position l_*. Equation (2.3) satisfies the required zero force condition at the free end of a cantilever, i.e. at $s_* = L$.

The steady hydrodynamic load per unit length experienced by the inverted flag is given by (2.2). As such, force equilibrium of the elastic sheet requires

$$\frac{\mathrm{d}^2\theta}{\mathrm{d}s^2} = -\kappa'\int_{s}^{1}|\sin\theta(l)|\sin\theta(l)\cos(\theta(s)-\theta(l))\,\mathrm{d}l, \tag{2.4}$$

where the dimensionless arc-length, $s \equiv s_*/L$ (and $l \equiv l_*/L$), is now used. The left-hand side of (2.4) is the local normalised restoring force of the elastic sheet at position, s, which is balanced by the hydrodynamic load on the right-hand side. The term under the absolute value sign in (2.4) accounts for the inherent symmetry in the sheet's deflection (it can deflect to up or down in figure 1*b*) and the dimensionless constant,

$$\kappa' \equiv \frac{\rho U^2 L^3}{D'}, \tag{2.5}$$

is the ratio of hydrodynamic to elastic restoring forces, which we shall refer to as the normalised flow speed: it is proportional to the speed squared (Sader *et al.* 2016). Here, $D' \equiv Eh^3/12$ is the flexural rigidity of the sheet, h is its thickness, and the boundary conditions for (2.4) are

$$\theta(0) = \left.\frac{\mathrm{d}\theta}{\mathrm{d}s}\right|_{s=1} = 0, \tag{2.6}$$

corresponding to the usual clamp ($s = 0$) and free end zero moment ($s = 1$) boundary conditions. The dash notation, i.e. κ', is used to distinguish this slender inverted flag problem from the previously studied large-aspect-ratio case (Sader *et al.* 2016); this difference is discussed in § 2.3. An equation similar to (2.4) was used previously to study the related problem of reconfiguration of a slender cantilevered rod of circular cross-section that is oriented perpendicular to the flow direction (Luhar & Nepf 2011); in the present case, the flow is parallel to the rod/blade.

Solution to (2.4) and (2.6) is obtained using a shooting method, where the angle at the cantilever free end, $\theta_{end} \equiv \theta(1)$, is adjusted to match the required clamp condition, $\theta_{clamp} \equiv \theta(0) = 0$; see (2.6). This is identical to the numerical procedure employed by Luhar & Nepf (2011), and utilises a finite difference discretisation of the integro-differential equation, (2.4) and (2.6). The numerics are implemented here in Mathematica and the discretisation is refined to achieve convergence better than 99.99 %; requiring $N \geqslant 200$ grid points on the interval, $0 \leqslant s \leqslant 1$.

Figure 2(*a*) gives results for θ_{clamp} as a function of θ_{end}, for various normalised flow speeds, κ'; equilibrium solutions correspond to the zeroes of θ_{clamp}, i.e. solutions that intersect the horizontal axis. These results are generated by varying θ_{end} and

https://doi.org/10.1017/jfm.2016.691 Published online by Cambridge University Press

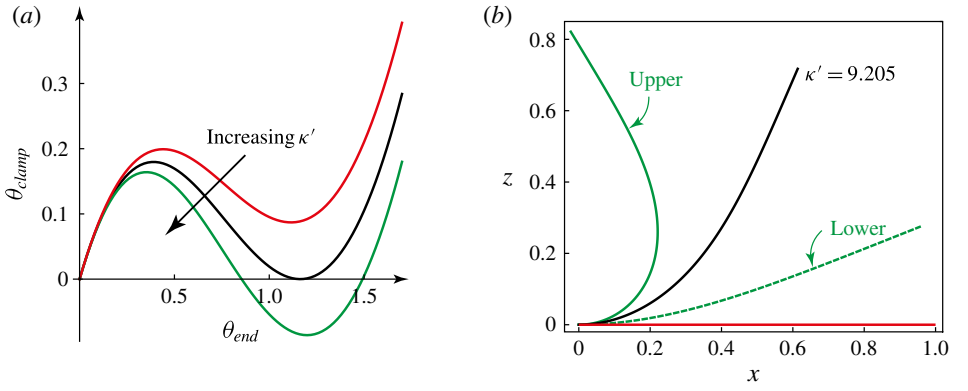

FIGURE 2. (Colour online) (*a*) Plot of θ_{clamp} versus θ_{end} for various normalised flow speeds: $\kappa' = 8.4$ (red); $\kappa' = 9.205$ (black); $\kappa' = 10.0$ (green). (*b*) Equilibrium deflection functions: zero-deflection equilibrium (red); deflected equilibrium at the critical flow speed $\kappa'_{critical} = 9.205$ (black); two distinct deflected equilibria for $\kappa' = 2\kappa'_{critical}$ (green). Upper deflection (solid green) increases in amplitude with increasing κ', while the lower deflection (dashed green) approaches the zero-deflection equilibrium (red horizontal line); see figure 3. Only positive angles are shown with negative angles having the same behaviour, by symmetry.

calculating θ_{clamp} using the above-specified numerical procedure. Only positive angles are presented in figure 2 for simplicity; negative angles have the same behaviour, by symmetry. The results in figure 2(*a*) show that only one equilibrium solution exists for small κ': $\theta_{end} = \theta_{clamp} = 0$, i.e. the zero-deflection equilibrium. This deflection function is illustrated in figure 2(*b*) (red horizontal line).

However, at the critical flow speed,

$$\kappa'_{critical} = 9.205, \tag{2.7}$$

a saddle-node bifurcation occurs and a new deflected equilibrium state is born with $\theta_{end} = 1.163 = 66.7°$; see the middle black curve in figure 2(*a*). To facilitate discussion, we henceforth refer to each symmetric pair of deflected states, for positive and negative θ, as a single deflected state. This new equilibrium is plotted in figure 2(*b*) (black curve). For $\kappa' > 9.205$, this equilibrium deflection splits into two distinct equilibria, one with $\theta_{end} > 66.7°$ (upper) and the other $\theta_{end} < 66.7°$ (lower) (as evident in the bottom green curve in figure 2*a*). These equilibrium deflection functions are plotted in figure 2(*b*) for $\kappa' = 2\kappa'_{critical}$ (green curves).

Figure 3 gives the bifurcation diagram for these equilibrium states, with the deflection angle θ_{end} plotted as a function of the normalised flow speed κ'. Note that other solutions exist for $\theta_{end} > \pi$, but the hydrodynamic model is not realistic in those cases because the sheet blocks the incoming flow: those solutions are regarded as unphysical.

2.2. *Stability of equilibrium states*

For $\kappa' > 9.205$, multiple equilibrium states exist for which their stability is now examined. We refrain from conducting a theoretical stability analysis because time-dependent hydrodynamic forces have not been calculated. Specifically, use

https://doi.org/10.1017/jfm.2016.691 Published online by Cambridge University Press

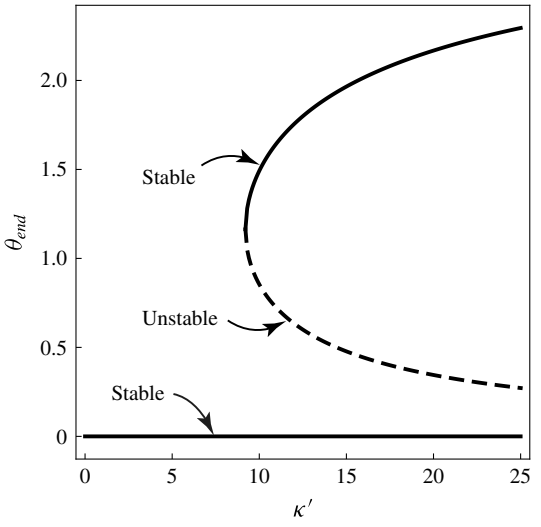

FIGURE 3. Bifurcation diagram of the cantilevered sheet's free end angle θ_{end} versus normalised flow speed κ'. Solid curves correspond to stable equilibria, dashed curves correspond to unstable equilibria. Only positive angles are shown: negative angles have the same behaviour, by symmetry.

of a time-averaged force (2.1) to model the inverted flag's behaviour implicitly assumes a steady flow. This is clearly not the case for the separated flow generated by the deflected equilibria, and (2.1) can only be used to calculate the existence and deflected shape of these equilibrium states. Stability of these states is determined here from general observations based on (i) the bifurcation diagram in figure 3, and (ii) a rigid sheet model system that mimics the behaviour of the inverted flag (in § 2.2.2).

2.2.1. *Observations from bifurcation diagram in figure 3*

The zero-deflection equilibrium of an inverted flag will be linearly stable in the limit of zero aspect ratio. This is because the hydrodynamic force (2.1) does not contain a linear dependence on the deflection angle for small angles.

From the bifurcation diagram in figure 3, the deflected equilibrium state of lower amplitude is expected to be unstable because it resides next to the linearly stable undeflected equilibrium. This lower deflected equilibrium defines the boundary of the basin of attraction for the undeflected equilibrium. For a similar reason, the higher-amplitude deflected equilibrium will be locally stable: the amplitude of this equilibrium increases with increasing flow speed, as may be expected intuitively; see figures 2(*b*) and 3. In contrast, the lower deflected equilibrium decreases in amplitude. These predictions are assessed experimentally in § 3.

2.2.2. *Rigid sheet model*

The stability and dynamics of the inverted flag can be modelled using the simplified configuration of a rigid slender sheet that is hinged at one end by a torsional spring of stiffness, k. This model is used to simplify analysis while capturing the dominant features of the inverted flag; it is of course also applicable to an inverted rod. The primary advantage is that the rigid sheet's angle of attack, $\theta(s) = \bar{\theta}$, is independent

https://doi.org/10.1017/jfm.2016.691 Published online by Cambridge University Press

of position, s, eliminating the need to explore the complete function space of $\theta(s)$ to determine the inverted flag's energy landscape; see below.

The normalised hydrodynamic force (torque) for this rigid sheet model is

$$f(\bar{\theta}) = \bar{\kappa}|\sin\bar{\theta}|\sin\bar{\theta}, \tag{2.8}$$

where $\bar{\kappa} \equiv \rho U^2 L^2 H/(2k)$ and is analogous to the normalised flow speed, κ', in (2.5) for the inverted (flexible) flag, which relates the hydrodynamic load to the elastic restoring force; equation (2.8) follows directly from (2.1). A formal relationship between $\bar{\kappa}$ and κ' does not exist due to the geometric difference between the two problems: this is irrelevant to our aim of investigating the stability/dynamics of the inverted flag by using this rigid sheet model. The overall dynamical system is

$$\frac{\mathrm{d}^2\bar{\theta}}{\mathrm{d}t^2} + \frac{1}{Q}\frac{\mathrm{d}\bar{\theta}}{\mathrm{d}t} + \bar{\theta} - \bar{\kappa}|\sin\bar{\theta}|\sin\bar{\theta} = F(\bar{\theta}, t), \tag{2.9}$$

where Q is the quality factor and gives the inverse scaled energy dissipation; t is scaled time and $F(\bar{\theta}, t)$ is an unspecified external applied force of zero mean in time, e.g. due to the unsteady hydrodynamic force arising from vortex shedding and any turbulence in the impinging flow. The first term in (2.9) corresponds to the sheet system's inertia and the third term its elastic restoring force. While damping is included in the second term of (2.9) for completeness, the quality factor, Q, is not used in the following analysis. Instead, we calculate the potential energy landscape of the sheet system to investigate its stability and discuss its dynamics.

In the absence of any flow, i.e. $\bar{\kappa} = 0$, equation (2.9) gives a standard linear damped harmonic resonator. The time-averaged hydrodynamic force in (2.8), $f(\bar{\theta})$, modifies the rigid sheet's dynamics by changing the system's local stiffness. This can clearly affect the equilibrium states of the system because $f(\bar{\theta})$ depends nonlinearly on the deflection angle, $\bar{\theta}$.

To determine these equilibrium states, and gain insight into their stability, we calculate the potential energy function for the dynamical system (2.9):

$$V(\bar{\theta}) = \frac{1}{2}\bar{\theta}^2 - \frac{\bar{\kappa}}{2}\left|\bar{\theta} - \frac{1}{2}\sin 2\bar{\theta}\right|, \tag{2.10}$$

which is plotted in figure 4. This shows that for $\bar{\kappa}$ values above bifurcation ($\bar{\kappa} > 1.38$), multiple equilibrium states exist; given by minima and maxima of $V(\bar{\theta})$. The zero- and large-amplitude equilibria are locally stable (minima of $V(\bar{\theta})$), while the lower-amplitude deflected equilibrium is unstable (maxima): this agrees with the discussion based on the bifurcation diagram in figure 3.

Dynamics on the energy landscape in figure 4 are governed by damping in the system and the time-dependent nature of the forcing term, $F(\bar{\theta}, t)$. Since these cannot be easily modelled, the specific dynamics cannot be determined completely. Nonetheless, figure 4 shows that the energy minimum of the large-amplitude equilibrium depresses below that of the zero equilibrium as $\bar{\kappa}$ increases. For $\bar{\kappa} > \pi/2$, the large-amplitude equilibrium exhibits a global potential energy minimum and is therefore energetically favourable; this value for $\bar{\kappa}$ is only slightly larger than the value at bifurcation, i.e. $\bar{\kappa} = 1.38$. The $\bar{\theta}$ value of this equilibrium rises in magnitude with increasing $\bar{\kappa}$, while that for the lower unstable deflected equilibrium approaches zero; the energy barrier for the undeflected equilibrium (local maximum in the potential energy) decreases in magnitude. As such, residence at the large-amplitude equilibrium

https://doi.org/10.1017/jfm.2016.691 Published online by Cambridge University Press

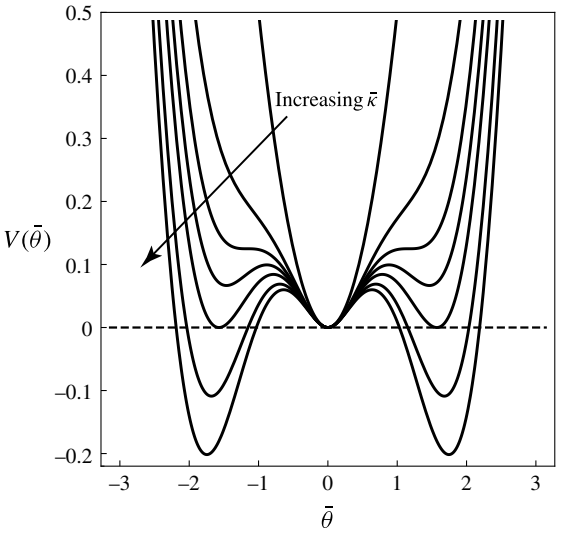

FIGURE 4. Potential energy function, $V(\bar{\theta})$, of the rigid sheet model system (2.9) for $\bar{\kappa} = 0, 1.2, 1.38, 1.48, \pi/2, 1.7, 1.8$ (increasing from centre outwards); saddle-node bifurcation occurs at $\bar{\kappa} = 1.38$. Equilibrium states corresponding to stationary points of the potential energy function. In contrast to figures 2 and 3, both positive and negative angles are given.

is favoured over the zero-deflection equilibrium as $\bar{\kappa}$ increases. For values of $\bar{\kappa}$ immediately above bifurcation, intermittent dynamics may be expected as the state of the system moves between the locally stable minima (they exhibit similar potential energies). This behaviour should be strongly dependent on the initial conditions and its existence is assessed experimentally in § 3.2.3.

2.3. *Critical normalised flow speed for arbitrary aspect ratios*

The calculation in § 2.1, and discussion in the previous section, show that an inverted flag of vanishingly small aspect ratio, $H/L \to 0$, exhibits a saddle-node bifurcation at

$$\kappa' = \kappa'_{small} = 9.205, \tag{2.11}$$

and can thus deflect to a new equilibrium.

In the opposite limit of large aspect ratio, $H/L \gg 1$, Sader *et al.* (2016) showed that a divergence instability occurs when

$$\kappa \approx \kappa_{large}\left(1 + \frac{2L}{H}\right), \tag{2.12}$$

where $\kappa \equiv \kappa'(1-\nu^2)$, ν is Poisson's ratio of the sheet and

$$\kappa_{large} = 1.85. \tag{2.13}$$

Note that definition of the normalised flow speed, κ, used for the large-aspect-ratio case by Sader *et al.* (2016), differs from κ' and we maintain this previous definition in the present calculation. As such, equation (2.11) becomes

$$\kappa_{small} = 9.205(1-\nu^2). \tag{2.14}$$

https://doi.org/10.1017/jfm.2016.691 Published online by Cambridge University Press

A Padé approximant is then constructed for the reciprocal of κ, connecting solutions for small and large aspect ratio, H/L. This yields the required result that is valid for all aspect ratios,

$$\kappa \approx \kappa_{large} \frac{\kappa_{small} + (\kappa_{small} - \kappa_{large}) \dfrac{H}{2L}}{\kappa_{large} + (\kappa_{small} - \kappa_{large}) \dfrac{H}{2L}}, \tag{2.15}$$

where κ_{large} and κ_{small} are given in (2.13) and (2.14), respectively.

The zero-deflection equilibrium is always linearly stable in the limit of zero aspect ratio, but its basin of attraction progressively shrinks as the flow speed increases above the bifurcation point. This is evident in figure 3 which shows that the free end angle, θ_{end}, for the unstable deflected equilibrium (dashed curve) approaches the zero-deflection equilibrium, $\theta_{end} = 0$, with increasing flow speed. As such, fluctuations in the flow due to vortex shedding or turbulence in the free stream can cause the flag to deflect and move away from the zero-deflection equilibrium, as discussed in § 2.2.2. Equation (2.14), and hence (2.15), must therefore be considered to be lower bounds. Precise experimental resolution of the flow speed where bifurcation occurs requires placing the inverted flag at a number of different initial positions, which we explore in § 3.2.

3. Measurements of inverted flags

The theoretical models in § 2 are now compared with (i) experimental data reported by Sader *et al.* (2016) for the critical flow speed at which bifurcation occurs, over a wide range of sheet aspect ratios, and (ii) new measurements on slender inverted flags. The latter measurements are designed to rigorously test the above theoretical predictions of stability and intermittent dynamics of slender flags.

3.1. *Comparison with measurements of Sader et al. (2016)*

Good agreement between measurements and (2.12) was reported in figure 6 of Sader *et al.* (2016) for sheets of large aspect ratio ($H/L > 1$). Equation (2.12) describes the critical flow speed where the destabilising linear hydrodynamic lift force balances the elastic restoring force of the sheet, i.e. where a divergence instability occurs. However, a strong discrepancy between (2.12) and measurements was reported for aspect ratios less than unity. It was suggested that a nonlinear vortex lift mechanism may be responsible for the observed discrepancy, because this mechanism is known to dominate at small aspect ratios and can enhance lift (Anderson 1991). The formulas developed in § 2.3 rigorously account for such nonlinear lift; equation (2.14) is due to drag from a separated flow and, as such, the hydrodynamic force has a nonlinear dependence on the sheet's deflection.

This prediction of nonlinear lift is assessed in figure 5 by comparing the theoretical predictions of (2.12)–(2.15) with the data reported by Sader *et al.* (2016). In the asymptotic limits of large and small aspect ratio, equations (2.12) and (2.14) agree well with the experimental observations, respectively. Strikingly, equation (2.15) gives excellent agreement with measurements over the entire range of aspect ratios studied, the case for which it is derived. No fit parameters are used in this comparison.

This observed agreement provides strong evidence that the nature of the zero-deflection equilibrium's stability changes as the aspect ratio is reduced. The previously described divergence instability at large aspect ratio gives way to a saddle-node

https://doi.org/10.1017/jfm.2016.691 Published online by Cambridge University Press

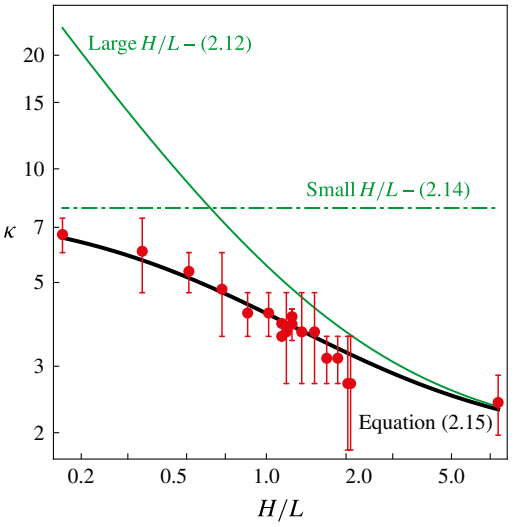

FIGURE 5. (Colour online) Comparison of measurements and theoretical predictions for the critical normalised flow speed at bifurcation, as a function of aspect ratio, H/L. Equation (2.12) (upper curve, large-aspect-ratio solution), equation (2.14) (horizontal line, small-aspect-ratio solution) and (2.15) (lower curve, globally valid Padé approximant).

bifurcation at low aspect ratio. The latter implies that the zero-deflection equilibrium of an inverted flag of zero aspect ratio is never locally unstable, though its basin of attraction decreases to a set of measure zero in the limit of large flow speed. As such, intermittent dynamics are expected across multiple locally stable equilibria (including the zero-deflection equilibrium) above the bifurcation point. These theoretically predicted features are yet to be observed experimentally. Their exploration and an assessment of the derived theory for slender inverted flags are the focus of the next section.

3.2. *New measurements of slender inverted flags*

While stability measurements of slender inverted flags were reported by Sader *et al.* (2016), the possible existence of multiple equilibria as predicted in § 2.1 was not explored. We therefore present a series of new measurements that aim to test for the presence of these equilibria, as well as give insight into the behaviour of flags of intermediate aspect ratios.

3.2.1. *Apparatus and measurement details*

The measurements are performed in an open-loop wind tunnel identical to that used by Kim *et al.* (2013) and Sader *et al.* (2016). A 10×10 square array of small fans generates uniform flow speeds ranging from 2.2 m s^{-1} to 8.5 m s^{-1} over a 1.2 m $\times$ 1.2 m test section. An aluminium honeycomb is used as a flow straightener to reduce transverse and axial fluctuations generated by the fans. The streamwise width of the honeycomb is 3.8 cm and the diameter of each cell in the honeycomb is 0.6 cm. The turbulence intensity, measured using a hotwire system, is $<8.2\,\%$ for the flow speeds studied. The maximum blockage ratio (for deflected sheets) in the data reported here is $<2.6\,\%$ for $H/L \leqslant 1$; it is $<4.4\,\%$ for $H/L \leqslant 1.7$. The flags are made of polycarbonate

https://doi.org/10.1017/jfm.2016.691 Published online by Cambridge University Press

($E = 2.41$ GPa, $\nu = 0.38$, $\rho_s = 1200$ kg m^{-3}) and have thicknesses of $h = 0.51$ and 0.76 mm with lengths of $L = 195$ and 300 mm, respectively. The aspect ratio of each flag is set by adjusting its height, H. The sheet's length is aligned horizontally whereas its height (i.e. span) is oriented vertically. The flag is clamped vertically at its trailing edge by an aluminium bar of square cross-section (width 12 mm) and its motion is filmed from above using a high-speed camera (Nanosense MKIII, Dantec Dynamics).

For flow speeds above the critical bifurcation speed, the deflected stable equilibrium position is taken as the average of a 30 s time series filmed at 100 f.p.s. Large-amplitude flapping occurs for aspect ratios $H/L \gtrsim 0.1$ (Sader *et al.* 2016). In these cases, the flag is damped to observe a deflected equilibrium; this is achieved by lightly touching the flag with a thin rigid pole (Sader *et al.* 2016). The flag position at each frame is detected using a Matlab script. The angle of the cantilevered sheet's free end at each equilibrium, θ_{end}, is measured from the slope at the end position. This is determined using a third-order polynomial fit to the deflected flag shape over the last 20 % of the flag length.

The existence of an unstable deflected equilibrium which is described in § 2 is assessed as follows. The initial position of the flag is adjusted by quasi-statically pushing it from the stable deflected equilibrium position towards the zero-deflection position using a thin and rigid pole of diameter $d = 3.175$ mm. Presence of an unstable deflected equilibrium must then lead to rapid and unassisted movement of the flag from the deflected initial condition towards the zero-deflection equilibrium. To measure this point at which the flag loses contact with the rigid pole, signalling entry into the basin of attraction of the zero-deflection equilibrium, the flag is coated with conductive paint and the pole is electrified. This forms an electric circuit with the flag–pole system acting as the switch. The deflected shape of the sheet at the time of loss of contact with the pole is taken to be the unstable deflected equilibrium.

The resonant frequency of the zero-deflection equilibrium is measured by fitting a two term Gaussian to the fast Fourier transform of a 270 s time series taken at 30 f.p.s. The second Gaussian is necessary to account for the presence, in certain cases, of another resonance peak of relatively small amplitude. This secondary peak is presumably due to weak nonlinear (viscoelastic) effects in the polycarbonate sheet. No time dependence is observed in the deflected stable equilibrium shapes, confirming that any viscoelastic properties exert a weak effect.

3.2.2. *Multiple equilibrium states of the flag*

The new measurements indeed verify the existence of multiple equilibrium states, as predicted theoretically in § 2.1. Figure 6 shows the measured angle of the cantilevered sheet's free end at the stable and unstable deflected equilibria. Measurements from several flags of varying small aspect ratios are presented, together with the theoretical predictions of § 2.1. As the aspect ratio is reduced (left-to-right and top-to-bottom in figure 6), both the measured critical bifurcation flow speed κ'_{small} and the free end angle θ_{end} increase, shifting towards the theoretical ($H/L \to 0$) curve of § 2.1. While there are some differences, even at the smaller aspect ratios, the measurements clearly approach the theoretical asymptotic solution as H/L is reduced.

Interestingly, the measurements reported in figure 6 systematically underestimate the $H/L \to 0$ asymptotic theory. This may be due, in part, to twisting of the flag which is observed to always occur when the flag deflects from its zero-deflection equilibrium. This twisting deformation is shown in figure 7 and exhibits a commensurate downward displacement of the flag. Large deformation of elastic beams inevitably results in coupling between bending and torsion, if the load or beam is not perfectly symmetric

https://doi.org/10.1017/jfm.2016.691 Published online by Cambridge University Press

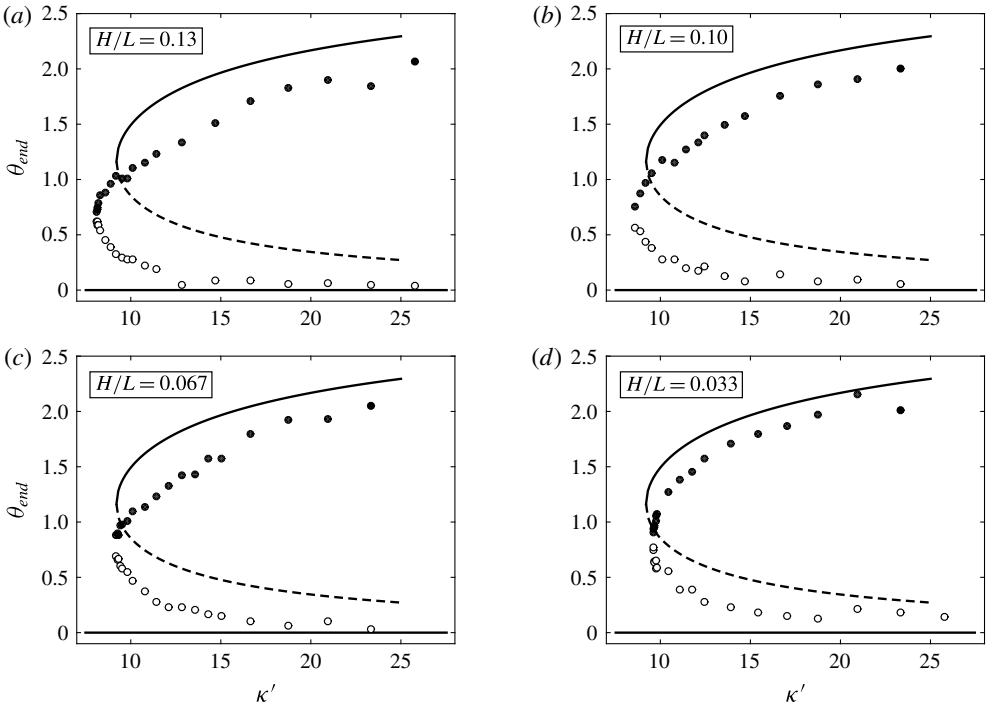

FIGURE 6. Measured free end angle, θ_{end}, at the stable (●) and unstable (○) deflected equilibria for aspect ratios of (*a*) $H/L = 0.13$, (*b*) $H/L = 0.10$, (*c*) $H/L = 0.067$, (*d*) $H/L = 0.033$. Theoretical prediction using the $H/L \to 0$ asymptotic theory of § 2.1 is given for stable (upper solid curve) and unstable (dashed curve) equilibria. Zero-deflection equilibrium position is shown for reference (horizontal solid line).

about the beam's major axis (Landau & Lifshitz 1970). Strikingly, every inverted flag studied here deforms in precisely the same manner, with the free end deflecting vertically downward in the gravity direction, demonstrating that gravity is a major factor in providing a symmetry break. When the flags are deflected sideways by applying a horizontal force with a stiff thin pole and the bank of fans are turned off, i.e. no flow, the large-amplitude twisting shown in figure 7 is not observed, suggesting that the initial break in symmetry is small. The resulting small twist, however, appears sufficient to modify the aerodynamics of the flag such that an additional torsional aerodynamic force is generated, resulting in a large twisting deformation. This coupled bending/twisting deformation is expected to reduce the drag experienced by the inverted flag because the flag now presents an angled face to the incoming flow. Such drag reduction reduces the maximum deflection angle of the inverted flag for a given flow speed, consistent with the observations reported in figure 6. While nonlinear coupling between bending and twisting under a gravitational load can be calculated, this complexity detracts from the principal aim of this study which is to describe the dominant stability mechanisms of slender inverted flags. The experimental angles reported in figure 6 are measured by observing the flag from above, and as such, they correspond to the projection of the deflection angle on the horizontal plane.

Bollay's 1939 calculations indicate that the normal force experienced by a rigid and flat blade of small but finite aspect ratio contains a term proportional to $\sin^2\theta$

https://doi.org/10.1017/jfm.2016.691 Published online by Cambridge University Press

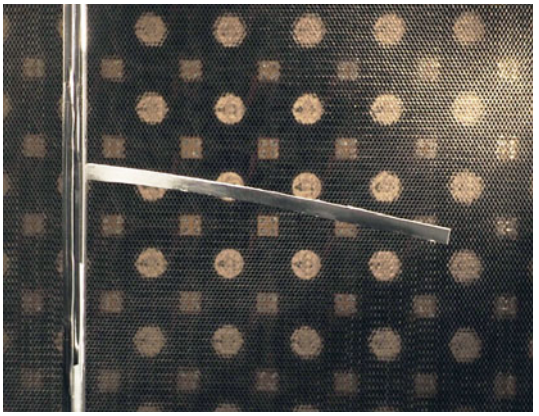

FIGURE 7. (Colour online) Photograph of slender inverted flag showing the combined flexural bending and twisting at large flow speeds, under the influence of gravitational and hydrodynamic loading; $H/L = 0.033$, $\kappa' = 16.6$. The bank of computer fans is visible with the flow direction out of the page. The flag is deflected strongly to the right relative to the flow direction, exhibiting a twist about its major axis together with commensurate bending in both the horizontal and vertical directions. The supporting aluminium bar is oriented in the vertical direction.

and one proportional to $\sin 2\theta$. These terms correspond to a Newtonian type (drag) law for zero aspect ratio and a linear lifting force for a blade of finite aspect ratio, respectively. As such, a small but measurable linear lift component is expected, which may contribute to the observed differences between measurement and theory in figure 6. This mechanism acts in addition to the reduction in drag due to twisting, and its presence and strength are explored using independent measurements in § 3.2.4.

Measurements by Sader *et al.* (2016) found no evidence for the existence of the multiple equilibria reported in figure 6. However, their study focused primarily on flags of large aspect ratio, H/L. It is therefore important to determine the aspect ratio at which the multiple equilibria emerge. A systematic experimental investigation using the present setup reveals that these multiple equilibria occur only for $H/L < 1.7$. Figure 8 gives the measured bifurcation diagram, i.e. the stable and unstable equilibrium end angles, θ_{end}, as a function of the normalised flow speed, κ', for several aspect ratios, H/L, in this range.

The linear component of the hydrodynamic force described above, i.e. the $\sin 2\theta$ term, is expected to increase in strength with increasing aspect ratio. Unlike the limiting case of $H/L \to 0$ where the zero-deflection equilibrium is always linearly stable, this additional linear component will cause the zero-deflection equilibrium of finite aspect ratio flags to become linearly unstable at finite flow speed. This behaviour is evident in figure 8, where the unstable deflected equilibrium branch (dashed curves) crosses the zero axis, causing the zero-deflection equilibrium to become linearly unstable. The critical κ' value at which this crossing occurs decreases as H/L is increased, as would be expected for an increasing linear component of the normal force. Indeed, this observed decrease in the unstable equilibrium's free end angle θ_{end} at bifurcation, with increasing H/L (see figure 8), is consistent with the large-aspect-ratio theory of Sader *et al.* (2016): for large H/L, the deflected unstable equilibrium does not exist and a divergence instability of the zero-deflection equilibrium occurs.

https://doi.org/10.1017/jfm.2016.691 Published online by Cambridge University Press

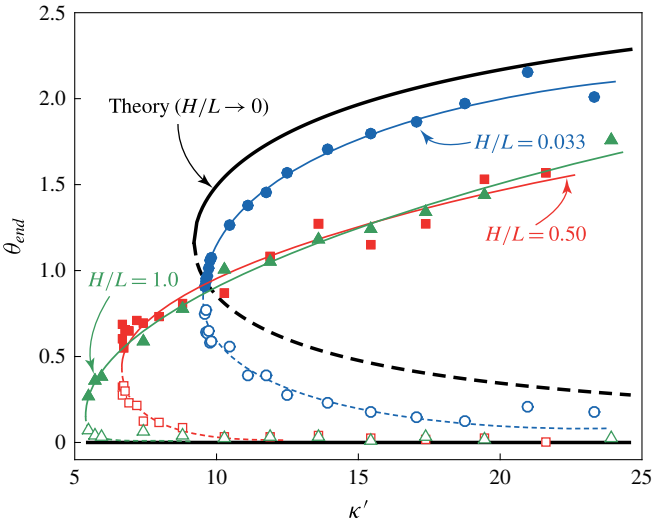

FIGURE 8. (Colour online) Measured free end angle, θ_{end}, of inverted flags at their stable (●) and unstable (○) deflected equilibria as a function of the normalised flow speed, κ'. Measurements shown for flags of aspect ratios of $H/L = 0.033$ (blue circle), $H/L = 0.50$ (red square) and $H/L = 1.0$ (green triangle). To guide the eye, fit curves to these measured data points are provided for each aspect ratio. Theoretical prediction is given for the limiting case of $H/L \to 0$ (solid black curves: stable equilibria; dashed black curve: unstable equilibrium). Undeflected shape (zero angle) is the horizontal black line.

3.2.3. *Intermittent dynamics at moderate flow speeds*

The rigid sheet model in (2.9) does not explicitly account for the effects of nonlinear damping or unsteady hydrodynamic forces, such as those produced by vortex shedding and turbulence in the flow; these are lumped into the unspecified forcing term $F(\bar{\theta}, t)$. Therefore, it does not completely model the dynamics of the rigid sheet (and inverted flag). However, equation (2.9) does prove useful in gaining a qualitative understanding of the inverted flag's stability and dynamics. For small values of $\bar{\kappa}$, the secondary potential well at finite $\bar{\theta}$ (corresponding to the stable deflected equilibrium) is shallow; see figure 4. This suggests that residence at this minimum is energetically unfavourable and small fluctuations in the flow will drive the flag away from the stable deflected equilibrium. This behaviour is now investigated experimentally, movies for which are provided in supplementary materials available at https://doi.org/10.1017/jfm.2016.691.

Figure 9(*a*) shows the variation in time of the non-dimensional displacement of the flag's free end, A/L, for $\kappa' = 9.2$. This flow speed is just above the bifurcation point where the two deflected equilibria emerge in measurements. Initially, the flag fluctuates around the zero-deflection equilibrium. Using a thin and rigid pole (as described in § 3.2.1), the flag is pushed (dashed red curve) to the stable deflected equilibrium position where it is released. The flag then resides at that position for finite time ($\approx$25 s) until it abruptly, and of its own accord, falls back into the zero-deflection position; also see the accompanying movie (supplementary materials). This observation is consistent with the energetic picture in figure 4 where fluctuations in the flow are expected to result in intermittent dynamics.

As $\bar{\kappa}$ is increased in the model system, its deflected energy minimum depresses below the zero-deflection energy minimum; see figure 4. Physically, this lets small

https://doi.org/10.1017/jfm.2016.691 Published online by Cambridge University Press

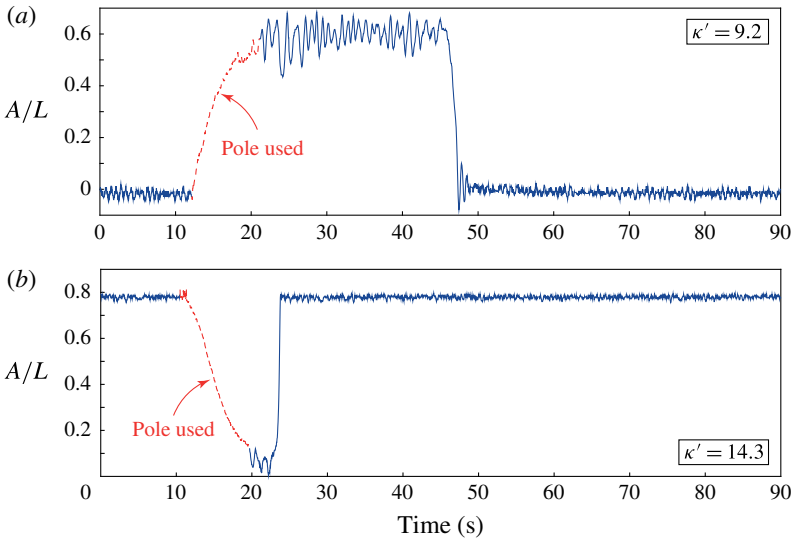

FIGURE 9. (Colour online) Measured dimensionless free end displacement A/L of an inverted flag as a function of time, for normalised flow speeds of (*a*) $\kappa' = 9.2$ and (*b*) $\kappa' = 14.3$. Aspect ratio $H/L = 0.067$. The flag is shifted to a different equilibrium using a thin rigid pole (red dashed curve) and then released.

fluctuations drive the flag from the zero-deflection equilibrium towards the (more energetically favourable) deflected equilibrium. A measurement under this scenario is shown in figure 9(*b*), corresponding to a normalised flow speed of $\kappa' = 14.3$; a movie is also provided (supplementary materials). The flag, initially oscillating around the deflected equilibrium, is forced (dashed red curve) with the thin pole to the zero-deflection position where it is again released. The flag then resides briefly (≈3 s) at the zero-deflection position before returning suddenly and unaided to the deflected equilibrium position. We remind the reader that the above-reported intermittency is expected to depend on fluctuations due to unsteady vortex shedding and on the level of turbulence in the impinging flow, with increased movement between multiple equilibrium states as the turbulence level is raised. Exploration of this effect presents an interesting area for further work.

As mentioned above, the flag exhibits oscillations about both the zero-deflection ($A/L = 0$) and deflected ($A/L > 0$) equilibria in these measurements. Intriguingly, the deflected equilibrium's oscillation amplitude is different in figure 9(*a*,*b*), with larger oscillations occurring at the lower flow speed (in figure 9*a*). This is expected because the energy minimum at the deflected equilibrium is shallower at the lower flow speed (as discussed above), allowing time-dependent fluctuations in the flow to more strongly perturb the sheet from this equilibrium position.

The zero-deflection equilibrium exhibits reversed behaviour, with larger oscillations being observed at the higher flow speed in figure 9(*b*). This is again explained by the energy landscape in figure 4, as the zero-deflection equilibrium's energy minimum is shallower at higher flow speeds, behaviour opposite to that of the deflected equilibrium's energy minimum.

Therefore, the observed oscillation amplitudes of the zero-deflection and deflected equilibria are entirely consistent with their intermittent dynamics discussed above.

https://doi.org/10.1017/jfm.2016.691 Published online by Cambridge University Press

3.2.4. *Presence of a linear hydrodynamic lift force at finite aspect ratio*

We now examine whether a linear lift force indeed exists for inverted flags of small but finite aspect ratio, as suggested by the results of § 3.2.2. This is achieved by performing independent measurements of the natural resonant frequency of the inverted flags at their zero-deflection equilibrium positions, as a function of aspect ratio.

When a slender inverted flag is placed at its zero-deflection equilibrium at finite flow speed, it is observed to resonate with small amplitude; see figure 9. For such small amplitudes, the quadratic (fourth) term on the left-hand side of the rigid sheet model system (2.9), which holds formally in the limit $H/L \to 0$, is small relative to the linear (third) term, provided $\bar{\kappa}$ is not large. The equation of motion for a damped harmonic resonator is then recovered. This equation depends on $\bar{\kappa}$ only through variations in the normalised damping coefficient, $1/Q$, and the external applied (hydrodynamic) force, $F(\bar{\theta}, t)$. These variations can both generally be considered negligible for small oscillation amplitudes. The resonant frequency of the flag is therefore independent of $\bar{\kappa}$ in this zero-aspect-ratio limit.

For small but finite aspect ratio ($H/L \ll 1$), however, the hydrodynamic force on the rigid sheet (and flag) includes a linear term, as discussed above (Bollay 1939). In addition to the nonlinear lift specified by (2.1) for a rigid slender blade, a linear normal lift force coefficient per unit length of the form $C_N = 2c \sin\theta \cos\theta$ arises, as discussed in § 3.2.2. Here, $c = 0$ in the zero-aspect-ratio limit ($H/L \to 0$) and is an increasing function of aspect ratio. Equation (2.9) thus takes the modified form,

$$\frac{\mathrm{d}^2\bar{\theta}}{\mathrm{d}t^2} + \frac{1}{Q}\frac{\mathrm{d}\bar{\theta}}{\mathrm{d}t} + \bar{\theta} - c\bar{\kappa}\sin\bar{\theta}\cos\bar{\theta} - \bar{\kappa}|\sin\bar{\theta}|\sin\bar{\theta} = F(\bar{\theta}, t). \tag{3.1}$$

For small oscillations around the zero-deflection equilibrium, this equation can be linearised to give

$$\frac{\mathrm{d}^2\bar{\theta}}{\mathrm{d}t^2} + \frac{1}{Q}\frac{\mathrm{d}\bar{\theta}}{\mathrm{d}t} + (1 - c\bar{\kappa})\bar{\theta} = F(\bar{\theta}, t). \tag{3.2}$$

This shows that the resonant frequency of the rigid sheet system (and an inverted flag) of small but finite aspect ratio, H/L, varies with the square root of $1 - c\bar{\kappa}$. Since c increases with increasing aspect ratio, larger-aspect-ratio sheets are expected to display a more significant reduction in their resonant frequency with increasing $\bar{\kappa}$.

Figure 10 gives the measured oscillation frequency of the zero-deflection equilibrium for several flags, as a function of the normalised flow speed κ' and aspect ratio H/L. Although the dependence on κ' is not necessarily linear, a linear fit is provided to facilitate comparison. The measured rates of decrease in frequency are -0.15, -0.12, -0.10 and -0.075 Hz for aspect ratios of $H/L = 0.13$, 0.10, 0.067 and 0.033, respectively. This verifies the above physical picture: a linear lift force exists for finite aspect ratio and its magnitude increases with increasing aspect ratio.

A significant reduction in frequency as flow speed increases is observed even for the smallest aspect ratio of $H/L = 0.033$. This indicates that linear lift affects the flag's dynamics at this small aspect ratio. This finding is consistent with figure 8, where a difference is always observed between the $H/L \to 0$ theory of § 2.1 and measurements at finite aspect ratio, even for the smallest aspect ratio of $H/L = 0.033$. As discussed, this mechanism acts in addition to twisting of the flag due to the combined effects of gravity and hydrodynamic loading, which leads to a reduction in deflection.

https://doi.org/10.1017/jfm.2016.691 Published online by Cambridge University Press

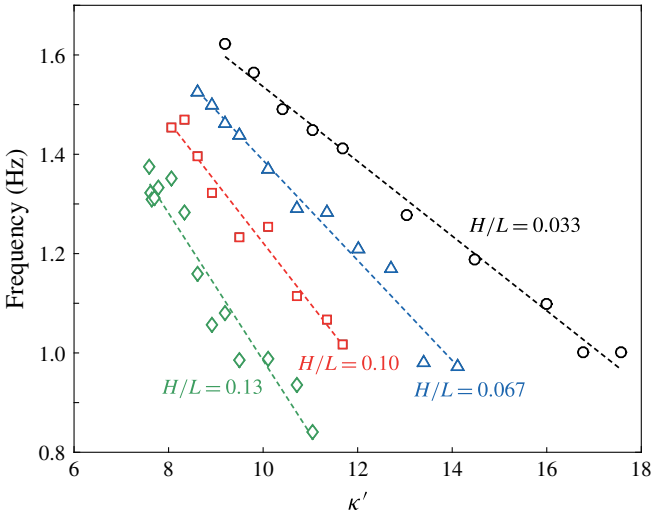

FIGURE 10. (Colour online) Natural frequency of oscillation of the zero-deflection equilibrium for inverted flags with aspect ratios of $H/L = 0.033$ (○), $H/L = 0.067$ (△), $H/L = 0.10$ (□) and $H/L = 0.13$ (◇). Linear fits to each data set are provided (dashed lines).

4. Application to inverted rod of Rinaldi & Paidoussis (2012)

Rinaldi & Paidoussis (2012) examined the stability of slender inverted rods of circular cross-section in a steady uniform flow. They theoretically predicted that the rods exhibit a divergence instability with increasing flow speed, but found poor agreement between theory and measurement; see § 1. Here, we extend and apply the theory derived in § 2.1 to their experiment. The present theory indicates that the inverted rod undergoes a saddle-node bifurcation, not divergence. This is identical to behaviour of the inverted flag. The measurements reported by Rinaldi & Paidoussis (2012) are compared with the predictions of this new model.

Unlike the inverted flag in figure 1, the inverted rod is oriented vertically (in the direction of gravity) with the rod's free end pointing downwards; the impinging flow is in the opposite direction. As such, the gravitational body force increases the effective stiffness of the rod. This effect is handled by including the gravitational body force in the equilibrium equation (2.3), leading to

$$\frac{\mathrm{d}^2\theta}{\mathrm{d}s^2} = G(1-s)\sin\theta - \kappa' \int_s^1 |\sin\theta(l)|\sin\theta(l)\cos(\theta(s)-\theta(l))\,\mathrm{d}l, \tag{4.1}$$

with the dimensionless gravity parameter given by

$$G \equiv \frac{\rho_s g A_s L^3}{EI}, \tag{4.2}$$

where ρ_s is the rod's density, $A_s = \pi R^2$ is its cross-sectional area, R is the rod radius, EI is its flexural rigidity which is defined in terms of the elastic properties and cross-section of the rod (Landau & Lifshitz 1970) and g is the gravitational acceleration. The normalised flow speed for this problem is

$$\kappa' = \frac{\rho U^2 L^3 R}{EI} C_D, \tag{4.3}$$

https://doi.org/10.1017/jfm.2016.691 Published online by Cambridge University Press

and $C_D = 1.1$ is the normalised drag coefficient for a circular cylinder (Taylor 1952).

Equation (4.1) is subject to the same boundary conditions as the inverted flag, i.e. (2.6), and is therefore solved in an identical manner. The gravitational body force will clearly increase the flow speed κ' at which bifurcation occurs, due to enhancement of the rod's effective stiffness. For the cylindrical rod considered by Rinaldi & Paidoussis (2012), gravity has a strong effect with a dimensionless gravity parameter of $G = 17.6$, based on their reported cylinder properties. In this case, the calculated flow speed where a saddle-node bifurcation occurs is $\kappa' = 26.7$, which is much larger than the numerical result for the slender inverted flag in (2.11). Stable and unstable equilibria are predicted to exist for higher flow speeds (not shown), as found for the inverted flag studied in §§ 2 and 3. At bifurcation, the angle at the rod's free end is also larger than that for the inverted flag and has a predicted value of $\theta_{end} = 75.5°$.

Rinaldi & Paidoussis (2012) use a dimensionless flow speed, $\bar{u}$, that is related to κ' by

$$\bar{u} = \sqrt{\frac{\pi R}{C_D L}}\kappa'. \tag{4.4}$$

Substituting the calculated critical value of $\kappa' = 26.7$ at bifurcation into (4.4) gives the required and equivalent result

$$\bar{u} = 1.23, \tag{4.5}$$

which can be compared directly to their measurements. Rinaldi & Paidoussis (2012) measure a value at bifurcation of $\bar{u} = 1.1$–1.7, and our theoretical prediction in (4.5) falls precisely in this range. This contrasts to the theoretical value for a divergence instability of $\bar{u} = 2.4$–2.7 that was reported by Rinaldi & Paidoussis (2012).

Further measurements are required to experimentally verify existence of stable and unstable equilibria of the inverted rod above this bifurcation point. Intermittent dynamics and stability are also expected, as observed for the inverted flag.

5. Conclusions

We have shown that the stability of a slender inverted flag in a steady uniform flow is markedly different to that of its large-aspect-ratio counterpart. While the latter exhibits a divergence instability as flow speed increases, the undeformed state of an infinitely slender inverted flag is always locally stable.

Specifically, a saddle-node bifurcation emerges at finite flow speed, giving rise to a deflected equilibrium state. This state splits into two equilibria at higher flow speeds, with the more strongly deflected one being stable and the weakly deflected one unstable. The unstable equilibrium defines the boundary of the basin of attraction for the undeflected flag, which vanishes in the limit of high flow speed. Inverted rods behave in an identical manner. The slender inverted flag theory presented here was combined with that for large aspect ratio (Sader *et al.* 2016), yielding a single formula for stability of the zero-deflection equilibrium (2.15) that is valid for all aspect ratios.

These theoretical predictions and formulas were compared with measurements of inverted flags and rods, where excellent agreement was observed throughout. Multiple stable and unstable equilibria for slender inverted flags were confirmed, as was the presence of intermittent dynamics resulting from the existence of these stationary states. The transition from a saddle-node bifurcation to divergence as the flag aspect ratio is increased was also clarified.

https://doi.org/10.1017/jfm.2016.691 Published online by Cambridge University Press

This study provides insight into the physics underlying the stability and motion of slender cantilevered structures in a uniform flow. It thus has direct application in understanding an array of biological processes, such as the dynamics of hairs, that are naturally slender.

Acknowledgements

This research was supported by the Gordon and Betty Moore Foundation, the Charyk Family Foundation, the Charyk Laboratory for Bio-Inspired Design, Caltech's Kavli Nanoscience Institute and the Australian Research Council grants scheme. C.H.-C. acknowledges support through the 'la Caixa' Fellowship Grant for Post-Graduate Studies, 'la Caixa' Banking Foundation, Barcelona, Spain.

Supplementary movies

Supplementary movies are available at https://doi.org/10.1017/jfm.2016.691.

REFERENCES

ANDERSON, J. D. 1991 *Fundamentals of Aerodynamics*. McGraw-Hill.

BATCHELOR, G. K. 1974 *An Introduction to Fluid Dynamics*. Cambridge University Press.

BLACKBURN, H. & HENDERSON, R. 1996 Lock-in behavior in simulated vortex-induced vibration. *Exp. Therm. Fluid Sci.* **12**, 184–189.

BOLLAY, W. 1939 A non-linear wing theory and its application to rectangular wings of small aspect ratio. *Z. Angew. Math. Mech.* **19** (1), 21–35.

DRELA, M. 2014 *Flight Vehicle Aerodynamics*. MIT.

ELOY, C., LAGRANGE, R., SOUILLIEZ, C. & SCHOUVEILER, L. 2008 Aeroelastic instability of cantilevered flexible plates in uniform flow. *J. Fluid Mech.* **611**, 97–106.

GABBAI, R. D. & BENAROYA, H. 2005 An overview of modeling and experiments of vortex-induced vibration of circular cylinders. *J. Sound Vib.* **282**, 575–616.

GILMANOV, A., LE, T. B. & SOTIROPOULOS, F. 2015 A numerical approach for simulating fluid structure interaction of flexible thin shells undergoing arbitrarily large deformations in complex domains. *J. Comput. Phys.* **300**, 814–843.

GOLDSTEIN, S. 1965 *Modern Developments in Fluid Dynamics*. Dover.

GURUGUBELLI, P. S. & JAIMAN, R. K. 2015 Self-induced flapping dynamics of a flexible inverted foil in a uniform flow. *J. Fluid Mech.* **781**, 657–694.

JONES, J. T. 1990 *Wing Theory*. Princeton University Press.

KIM, D., COSSÉ, J., HUERTAS CERDEIRA, C. & GHARIB, M. 2013 Flapping dynamics of an inverted flag. *J. Fluid Mech.* **736**, R1.

KORNECKI, A., DOWELL, E. H. & O'BRIEN, J. 1976 On the aeroelastic instability of two-dimensional panels in uniform incompressible flow. *J. Sound Vib.* **47** (2), 163–178.

LANDAU, L. D. & LIFSHITZ, E. M. 1970 *Theory of Elasticity*. Pergamon.

LUHAR, M. & NEPF, H. M. 2011 Flow-induced reconfiguration of buoyant and flexible aquatic vegetation. *Limnol. Oceanogr.* **56**, 2003–2017.

PAIDOUSSIS, M. P., PRICE, S. J. & DE LANGRE, E. 2010 *Fluid-Structure Interactions: Cross-Flow Instabilities*. Cambridge University Press.

RINALDI, S. & PAIDOUSSIS, M. P. 2012 Theory and experiments on the dynamics of a free–clamped cylinder in confined axial air-flow. *J. Fluids Struct.* **28**, 167–179.

RYU, J., PARK, S. G., KIM, B. & SUNG, H. J. 2015 Flapping dynamics of an inverted flag in a uniform flow. *J. Fluids Struct.* **57**, 159–169.

SADER, J. E., COSSÉ, J., KIM, D., FAN, B. & GHARIB, M. 2016 Large-amplitude flapping of an inverted-flag in a uniform steady flow – a vortex-induced vibration. *J. Fluid Mech.* **793**, 524–555.

https://doi.org/10.1017/jfm.2016.691 Published online by Cambridge University Press

SCHMITZ, F. W. 1941 *Aerodynamics of the Model Airplane. Part 1. Airfoil Measurements*. Redstone Scientific Information Center.

SHELLEY, M. J. & ZHANG, J. 2011 Flapping and bending bodies interacting with fluid flows. *Annu. Rev. Fluid Mech.* **43**, 449–465.

TADRIST, L., SAUDREAU, M. & DE LANGRE, E. 2014 Wind and gravity mechanical effects on leaf inclination angles. *J. Theor. Biol.* **341**, 9–16.

TANG, C., LIU, N.-S. & LU, X.-Y. 2015 Dynamics of an inverted flexible plate in a uniform flow. *Phys. Fluids* **27**, 073601.

TAYLOR, G. I. 1952 Analysis of the swimming of long and narrow animals. *Proc. R. Soc. Lond.* A **214** (1117), 158–183.

THEODORSEN, T. 1935 General theory of aerodynamic instability and the mechanism of flutter. *NACA Rep.* **496**, 414–433.

WILLIAMSON, C. H. K. & GOVARDHAN, R. 2004 Vortex-induced vibrations. *Annu. Rev. Fluid Mech.* **36**, 413–455.

ZHANG, J., CHILDRESS, S., LIBCHABER, A. & SHELLEY, M. 2000 Flexible filaments in a flowing soap film as a model for one-dimensional flags in a two-dimensional wind. *Nature* **408**, 835–839.

https://doi.org/10.1017/jfm.2016.691 Published online by Cambridge University Press